

pubs.acs.org/JPCC Article

Simulating Segregation in a Ternary Cu-Pd-Au Alloy with Density Functional Theory, Machine Learning, and Monte Carlo Simulations

Published as part of The Journal of Physical Chemistry virtual special issue "Cynthia Friend Festschrift".

Yilin Yang, Zhitao Guo, Andrew J. Gellman, and John R. Kitchin*



Cite This: J. Phys. Chem. C 2022, 126, 1800-1808



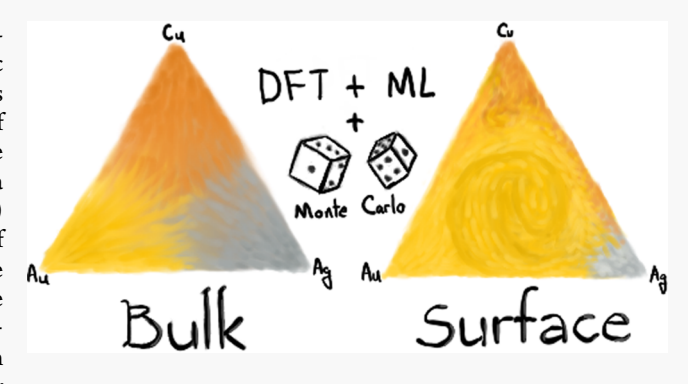
ACCESS I

Metrics & More

Article Recommendations

SI Supporting Information

ABSTRACT: Simulation of the segregation profile of multicomponent alloys is important to investigate the catalytic properties of alloy catalysts. Density functional theory (DFT) is too expensive to use directly to evaluate the potential energies of the slab configurations during the simulations. In this work, we build a neural network (NN) based on 5278 DFT calculations as a surrogate model to evaluate the potential energies of the fcc(111) slabs for a ternary Cu–Pd–Au alloy. The trained NN is capable of predicting the Cu–Pd–Au potential energies across the whole ternary space with high accuracy. Combining the NN with Monte Carlo simulation, we obtained the segregation profile of Cu–Pd–Au at 600 K across the bulk composition space. The simulation results are qualitatively consistent with the experimental data for



PdAu and CuAu, but they are incorrect along the PdCu line. Further DFT calculations show that the perfect fcc(111) slab is not capable of capturing the CuPd segregation behavior on undercoordinated surfaces under the realistic conditions.

INTRODUCTION

Alloys have a wide range of applications in chemical engineering for their versatile properties. For example, Pd based alloys are used in the hydrogen separation process. Pd has the ability to separate hydrogen from mixed industrial gases. However, pure Pd membranes suffer from hydrogen embrittlement and H₂S poisoning during the separation process, which can be mitigated in some bimetallic alloys, for example, with PdCu and PdAu. More recently, some studies have focused on using ternary alloys such as PdCuAu in the separation membrane.

The hydrogen separation process using Pd based alloys takes place in three main steps: dissociative adsorption, diffusion, and desorption. During this process, the surface concentration of the alloys plays an important role in the adsorption and desorption steps, while the bulk concentration influences the diffusion step. A desirable separation membrane requires an appropriate balance among adsorption activity, hydrogen permeability, mechanical stability, and poison resistance, which are also determined by the surface concentration and bulk concentration. Usually, the surface concentration differs from the bulk concentration in the alloys because of the surface segregation phenomenon. Therefore, investigation into the surface segregation is necessary for the design of the Pd based hydrogen separation membrane.

Another application of Pd based alloys is in the synthesis of vinyl acetate. 10,11 AuPd can increase the activity and the

selectivity of this reaction. More specifically, the activity and selectivity are determined by the surface coverage and the site distribution of Pd. Therefore, the study of surface segregation helps determine the mechanism of the catalytic reactions based on those metallic alloys. This is necessary to design these alloy catalysts with desired properties.

There are several experimental and theoretical methods that have been developed to study surface segregation. Most experimental approaches measure the surface concentration of alloy membranes using low-energy ion scattering spectroscopy (LEIS) and X-ray photoelectron spectroscopy (XPS), ^{12,13} and at each measurement, only one bulk concentration is investigated. Although high throughput methods have been used in some surface segregation experiments, the usage is still limited. ^{7,14–16}

With the limitations of experimental methods and the development of the computational capacity, the demand for theoretical study of surface segregation is growing constantly. Some simulation methods such as molecular dynamics¹⁷ and

Received: November 8, 2021 Revised: December 23, 2021 Published: January 19, 2022





Monte Carlo¹⁸ simulation have been adopted in the study of surface segregation. For higher accuracy, density functional theory (DFT) may also be applied to evaluate the potential energies of the alloy configurations during the simulation process.¹⁹ In general, simulations based on (semi)empirical methods such as embedded atom method (EAM) can simulate the surface segregation on large atomic systems but typically with lower accuracy, while simulations using DFT calculations are usually limited to small slabs although it has higher accuracy. Furthermore, most of these theoretical methods deal with bimetallic alloys; only a few simulations involve ternary alloys, and those use empirical potentials²⁰ or small slabs.²¹

Recently, machine learning potentials²² have become a hot topic in the atomic simulation field. Machine learning models such as k-nearest neighbors regression²³ and kernel ridge regression²⁴ can be trained with DFT potential energies of a small number of atomic configurations and then be used to evaluate the potential energies of new configurations. The appropriately trained machine learning potentials are much more computationally efficient than DFT while having similar accuracy with DFT under certain conditions.²⁵ Among machine learning models, the neural network (NN)²⁶ is now a standard method known for its flexibility and high accuracy. The effectiveness of the NN in the construction of potential energy surface for the alloys has been demonstrated in systems such as in PdAu alloys²⁷ and SiLi amorphous alloys.²⁸ Despite many examples of NN use for bimetallic alloys, its applications to ternary alloys are relatively rare.²⁹ There is an example of using a NN to study the surface properties of AuPd nanoalloy in aqueous solvents, which involves four different elements,3 where the NN also performed well.

In this work, we utilize a BPNN approach to develop a NN potential to simulate segregation in a ternary Cu–Pd–Au alloy across composition space. We generated a data set including 5278 DFT calculations to train and validate the NN. The training samples were shown to cover the G^2 fingerprint space for the PdCuAu ternary slab. The trained NN was then used with Monte Carlo simulation on a $10 \times 10 \times 15$ fcc(111) slab to model the surface segregation of this ternary alloy. The predicted surface concentrations were compared with the experimental results, and the discrepancy between them was analyzed by further DFT calculations and analysis.

METHODOLOGY

Density Functional Theory. The Vienna ab initio simulation package $(VASP)^{31,32}$ was used to conduct the DFT calculations in which the wave functions were represented by projector augmented wave (PAW) method. The Perdew–Burke–Ernzerhof generalized gradient approximation $(GGA-PBE)^{35,36}$ was chosen as the exchange–correlation functional. The density of k-points in the Monkhorst–Pack mesh³⁷ was approximately 5 per reciprocal angstrom, and the plane-wave energy cutoff was 400 eV. The convergence error from the chosen parameters mentioned above was around 2 meV/atom.

Experimental Data. The experimental data compared in this work is taken from ref 38. Composition spread alloy films (CSAFs) were used as a high-throughput method to accelerate the experimental process. Bulk composition and surface composition were characterized by energy-dispersive X-ray (EDX) and low-energy He⁺ ion scattering (LEIS), respectively. More details of the experimental conditions can be found in the original paper.

Neural Network. The Behler–Parrinello NN framework was used to evaluate the total potential energy of the surface slabs, of which the configurations were represented by the fingerprints of radial G^2 symmetry functions with η values of 0.05, 4, and 20. The cutoff radius was set as 6 Å to bound the range of the local environment around every atom. This value was reported with good results in alloys involving Pd, Cu, and Au. The NN framework in this work contains three independent NNs, one for each element: Pd, Au, and Cu. Each NN has the same structure of two hidden layers with ten neurons per layer. Thus, there are in total 221 parameters in each NN. The training and evaluating processes of the NNs on the PdCuAu surface slabs were conducted using the atomistic machine learning package $(AMP)^{41}$ in combination with the atomic simulation environment (ASE) package.

Training Samples across the G² Fingerprints Space. In this work, 5278 fcc(111) slabs were generated to train, validate, and evaluate the neural network. Six lattice constants ranging from 3.637 Å (of pure Cu) to 4.174 Å (of pure Au) and fcc(111) slabs of $1 \times 1 \times 7$, $2 \times 1 \times 7$, $\sqrt{3} \times \sqrt{3} \times 7$, $\sqrt{7} \times \sqrt{7} \times 5$, and 3 × 3 × 5 were used to generate these slabs. In total, 5100 slabs were generated randomly (with or without constraints on the bulk concentration; see details in the Supporting Information) as the training and validation data sets, with the split ratio of 9:1. Furthermore, to evaluate the generalization ability of the NN, 178 slabs of $\sqrt{12} \times \sqrt{12} \times 5$ were then randomly selected as the test set. Compared to the number of all possible configurations, which is more than 3⁴⁵ (45 is the number of atoms in the slab $3 \times 3 \times 5$), the size of the training and the validation set is small. The diversity of the training samples in the fingerprint space is analyzed in the following discussion.

Training samples spanning the fingerprint space are required to enable the NN to make accurate predictions with the various atomic local environments in the Monte Carlo simulation process across the composition space. For the ternary alloy PdCuAu, the G^2 fingerprints calculated by three different η values are in a nine-dimensional space, which is hard to visualize and sample. It turns out that features indicating the same surrounding element are highly correlated (see the Supporting Information). Thus, the training samples can be visualized and selected in the 3D space made up of the fingerprints calculated with a certain η .

In the system of fcc(111) surface slabs of the PdCuAu, the fingerprint space generated by a certain η and the cutoff radius of 6 Å contains several triangular planes in the 3D space. These planes are characterized by different lattice constants of the slab and the different locations of the atoms in the slab (surface, subsurface, and bulk). Figure 1 shows the G^2 fingerprints calculated with η of 0.05 for PdCuAu fcc(111) slabs with different lattice constants and structures. According to the formula of the G^2 symmetry function, the lattice constant of the slab and the position of the atom in the slab determine the plane subspace of the atomic fingerprints, while the composition of the atomic local environment determines the location of the fingerprints in the triangular plane. Quantitative analysis of the density of the points on the triangular planes can be found in the Supporting Information.

The fingerprints of the bulk atoms in the training set are illustrated in Figure 2, which shows that the fingerprints of the data set almost cover the whole triangular plane. With the difference lattice constants that determine the triangular planes

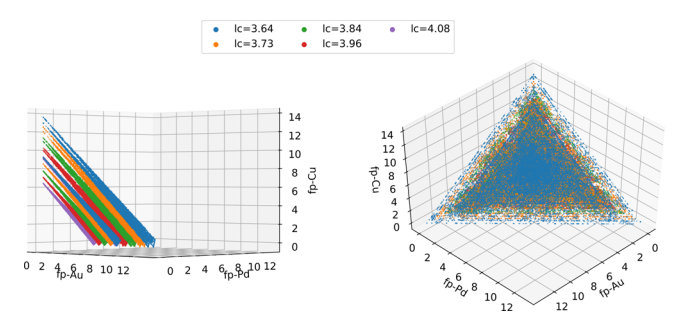


Figure 1. Fingerprints calculated by $\eta=0.05$ for surface slabs with different structures $(1\times 1\times 7,\ 2\times 1\times 7,\ \sqrt{3}\times \sqrt{3}\times 7,\ \sqrt{7}\times \sqrt{7}\times 5)$ and lattice constants (3.61 Å, 3.73 Å, 3.84 Å, 3.96 Å, and 4.08 Å). The x,y,z axes are the fingerprint values for different surrounding elements in the atomic local environment set by the cutoff radius. In the left plot, fingerprints of the same lattice constant are located in three planes, which represent the bulk, subsurface, and surface environments from top to bottom. In the right plot, fingerprints in the same plane are distributed around a triangle, where the three angles representing the local environments purely consist of three different elements.

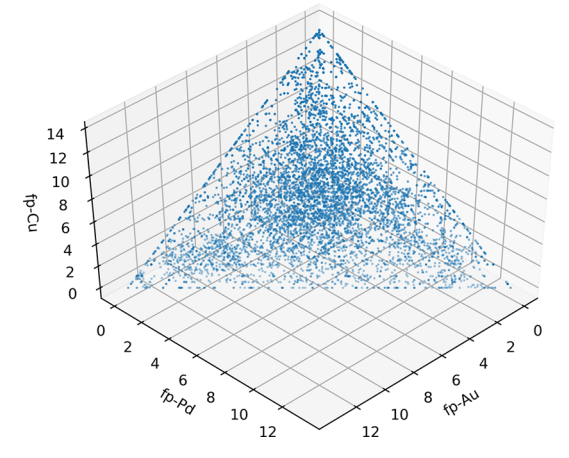


Figure 2. Fingerprints of bulk atoms in the training slabs with the lattice constant of 3.64 Å. The fingerprints in the figure were calculated with η of 0.05.

in the 3D space, the fingerprints of generated slabs have sampled across the whole fingerprint space of the PdCuAu fcc(111) slabs.

Monte Carlo Simulation. The Monte Carlo (MC) simulations were conducted on the slab fcc(111) $10 \times 10 \times 15$ whose lattice constant was estimated for the overall composition with Vegard's law. The potential energies of the generated configurations were evaluated by the trained NN. In the Monte Carlo simulation, a new configuration was accepted if the change in energy is negative. Otherwise, the new configuration was accepted with Boltzmann probability where the energy term was the potential energy change scaled by RT.

■ RESULTS AND DISCUSSION

Performance of Neural Network. We first show that the neural network was well trained with the 4590 selected fcc(111) slabs. Figure 3a illustrates the performance of the NN on the training set and the validation set. Both and training and validation sets have a mean absolute error (MAE) of around 2 meV/atom. The residual error distribution of the validation set is pretty similar to that of the training set, which means that

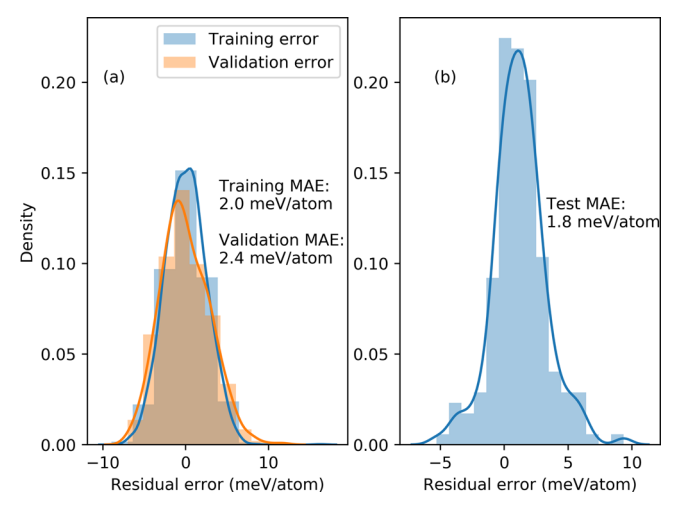


Figure 3. Distribution of the NN residual error on the training, validation, and test sets: (a) MAE and the residual error of the training and the validation sets which share the same distribution of the slab configurations; (b) MAE and the residual error of the test set which contains slabs with larger unit cell than the training data.

there was no apparent overfitting during the training process. The generalization ability of the NN was assessed by its performance on the larger $\sqrt{12} \times \sqrt{12} \times 5$ slab configurations. In the larger unit cell of this slab there can be a broader range of atomic local environments which are different from the training and validation sets. The performance of the NN on the generalization test set is shown in Figure 3b. Although there is some bias (nonzero mean residual error) on the NN predictions, the size of the MAE is still comparable with that of the training and validation sets. The bounded error of the NN on the generalization set supports the analysis of the fingerprints in the Supporting Information showing that 3 X 3 × 5 slabs are sufficient to span almost all atomic environments which are mainly determined by the first and second nearest neighbors of the central atoms. Therefore, we are confident that the trained NN also has the ability to predict the potential energies for larger slabs in the Monte Carlo simulation.

Monte Carlo Simulation Results. With the trained NN, 24 bulk concentrations across the whole ternary diagram were selected to conduct the MC simulations at a temperature of 600 K. There were a total 15 000 successful MC steps (atom swaps) on each bulk concentration, and the last 6000 steps were used to calculate the average surface concentration. Figure 4 shows a representative MC process on a bulk concentration of 20:23:47 for Pd:Cu:Au.

The MC simulation results for 24 bulk concentrations at a temperature of 600 K are shown in Figure 5. The values in the figures were calculated by subtracting bulk concentrations from the surface concentrations for each element. Therefore, positive values mean the segregation to surface (indicating an excess at the surface compared to the bulk) while negative values represent depletion from surface. In the simulation results, Pd is depleted from the surface at most bulk concentrations except the area near the PdCu binary alloy, where Pd segregates to the surface. For Cu, it is depleted from the surface at all bulk concentrations especially near the CuAu area. In contrast, Au segregated to the surface at all bulk concentrations. The simulated segregation tendencies are partially consistent with the reported simulation results using

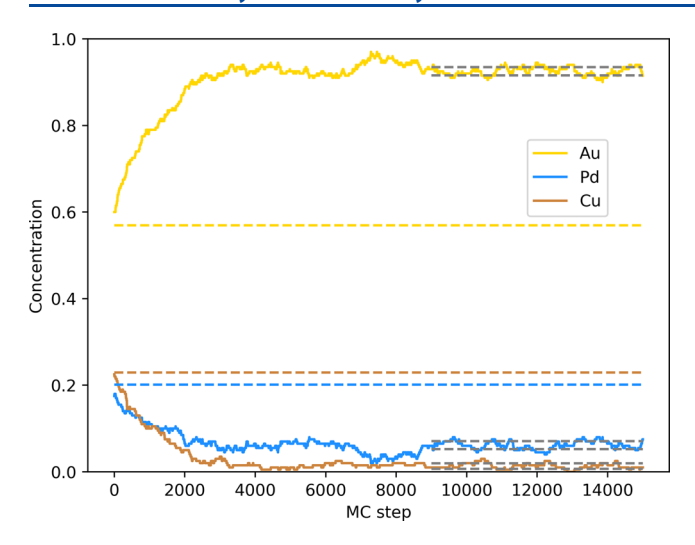


Figure 4. MC trajectory of the top layer concentration on a $10 \times 10 \times 15$ fcc(111) slab with bulk concentrations of 20:23:47 for Pd:Cu:Au over 15 000 successful steps. The colored dashed lines are the bulk concentrations, while the solid lines are the surface concentrations. The last 6000 steps were used to calculate the average surface concentration and the standard deviation which is represented by the gray dashed lines.

a cluster expansion.⁴⁵ Au is qualitatively observed to segregate to the surface at all compositions. There is an inconsistent segregation trend for Pd and Cu in their binary alloy compositions. Simulation predicts the segregation of Pd to the surface, whereas Pd is depleted from the surface in the experimental results. The second discrepancy is that the segregation ability of Cu is underestimated in the simulations and it is overestimated for Au.

To evaluate the segregation ability of Pd, Cu, and Au more quantitatively, the segregation energies for the binary combinations are calculated assuming each pair of two elements in equilibrium. More specifically, the reaction energies for the following three reactions are evaluated based on the simulation and experimental results:

$$\begin{array}{l} \operatorname{Au} \otimes \operatorname{Bulk} + \operatorname{Pd} \otimes \operatorname{Surf} \stackrel{K_{\operatorname{Au-Pd}}}{\longleftrightarrow} \operatorname{Pd} \otimes \operatorname{Bulk} + \operatorname{Au} \otimes \operatorname{Surf}; \\ \Delta G_{\operatorname{Au-Pd}} = -RT \, \ln \, K_{\operatorname{Au-Pd}} \\ \\ \operatorname{Au} \otimes \operatorname{Bulk} + \operatorname{Cu} \otimes \operatorname{Surf} \stackrel{K_{\operatorname{Au-Cu}}}{\longleftrightarrow} \operatorname{Cu} \otimes \operatorname{Bulk} + \operatorname{Au} \otimes \operatorname{Surf}; \\ \Delta G_{\operatorname{Au-Cu}} = -RT \, \ln \, K_{\operatorname{Au-Cu}} \\ \\ \operatorname{Pd} \otimes \operatorname{Bulk} + \operatorname{Cu} \otimes \operatorname{Surf} \stackrel{K_{\operatorname{Pd-Cu}}}{\longleftrightarrow} \operatorname{Cu} \otimes \operatorname{Bulk} + \operatorname{Pd} \otimes \operatorname{Surf}; \\ \Delta G_{\operatorname{Pd-Cu}} = -RT \, \ln \, K_{\operatorname{Pd-Cu}} \end{array}$$

These reactions are for the segregation of a certain element against another element from left to right. The K_i parameters in the equations represent the equilibrium constants for these reactions. For example, $K_{\rm A-B}$ is defined as c(B@Bulk)c(A@Surf)/[c(A@Bulk)c(B@Surf)]. These reaction energies $\Delta G_{\rm A-B}$ can be regarded as the relative segregation ability of A over B, and a negative value means the preferential segregation of A over B. Figure 6 shows the segregation energies of Au-Cu, Au-Pd, and Pd-Cu pairs. These data points have excluded the samples with bulk composition less than 0.2 and surface composition of 0 for the involved elements. Similar to the qualitative results above, the segregation energy for the Au-Pd pair based on the simulation is close to the experimental data (on parity), and a negative sign means that Au tends to segregate to the surface compared to Pd in this ternary system. The segregation energy for Au-Cu in the simulation is more negative than the experimental results, which means that the segregation tendency of Au over Cu is overestimated in the simulations. For Pd-Cu, the simulated segregation energy has the opposite sign compared to the experimental data, which illustrates an opposite segregation trend for these two

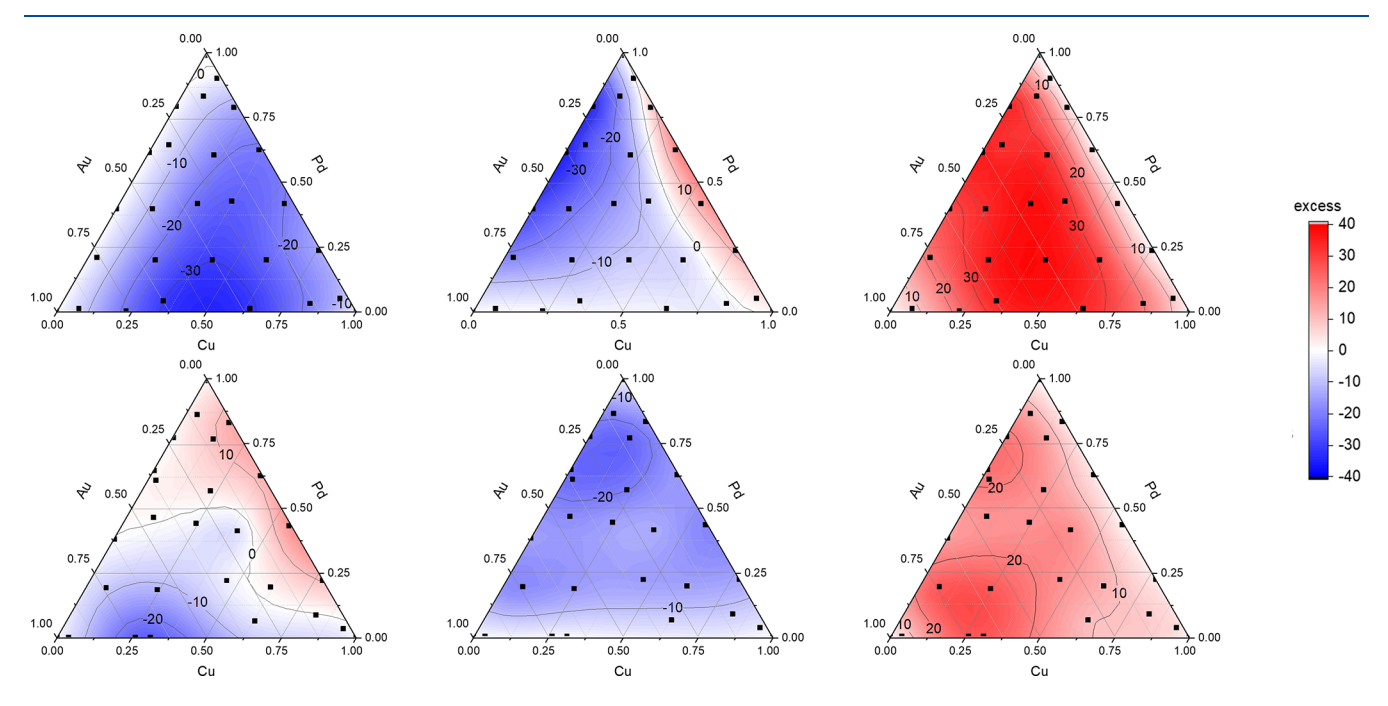


Figure 5. MC simulation results for 24 bulk concentrations at 600 K. These plots show the excess surface composition compared to the bulk composition for Cu, Pd, and Au. The first row is for the simulation results, while the second row shows the experimental results.

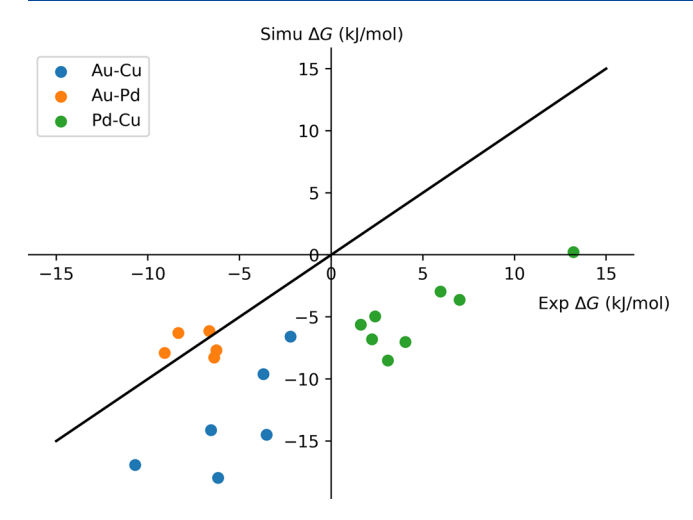


Figure 6. Segregation energies for Au–Cu, Au–Pd, and Pd–Cu pairs derived from simulation and experimental data. Each dot corresponds to a different bulk composition.

elements. These discrepancies between the simulation and experiment shall be discussed in the rest of this manuscript.

Phase Separation in Experiments. Before exploring any possible calculation factors that may be responsible for the discrepancies, we note that the MC method that we used is limited to simulation of one type of crystal system (fcc in our case). It has been reported that there exists a B2 phase in the phase diagram of the CuPd, which is not considered during the simulations in this work. This phenomenon actually affects the segregation profile of the alloy.³⁸ According to the experimental observations, the segregation of Cu over Pd is inhibited with the appearance of the B2 phase, and the affected bulk composition is in the range $0.4 < x_{Cu} < 0.7$. The Cu segregation is only reduced; however, it does not invert, so this is not likely to be an explanation for the discrepancy that we see in the simulations.

Role of Surface Relaxation. One of the possible reasons for the discrepancy between the simulation and experiment is the effect of surface relaxation. In previous work²⁷ we found that relaxation energies were not important in capturing segregation trends in Pd—Au because they largely cancel, and so we did not consider them here. It is possible that the larger size difference between Cu, Pd, and Au could be more relevant here.

To determine the impact of surface relaxation on these results, a $2 \times 2 \times 5$ fcc(111) slab was used to compare the potential energy before and after surface relaxation. The bottom three layers of the slab were set with the concentration of 1:1:1 for Au:Pd:Cu, and the lattice constant was fixed according to Vegard's law. 202 unique energy configurations were selected to be evaluated. Since the potential energy difference (ΔE) before and after atoms swap matters in the Monte Carlo simulation, we investigated this quantity in the 2 \times 2 \times 5 slab. Among 202 unique energy configurations, the ΔE s of 285 atom swaps in the top two layers were evaluated by NN and DFT. The ΔE calculated by the NN without surface relaxation, DFT energies with surface relaxation, and their pairwise difference $\Delta \Delta E$ are shown in the Figure 7. While the ΔE of every atom swap ranges from 0 to 1 eV, the difference of the ΔE calculated by NN without relaxation and DFT with relaxation is less than 0.2 eV, and most of them are less than 0.1 eV. More systematically, Figure 8 compares the ΔEs of

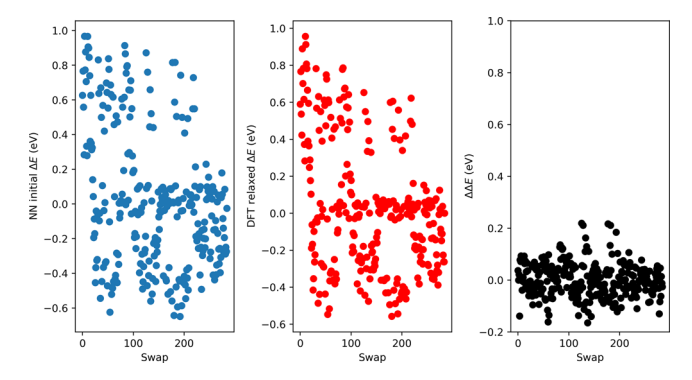


Figure 7. Potential energy difference before and after atomic swaps calculated by NN without surface relaxation (left) and DFT with surface relaxation (middle) as well as their pairwise difference (right).

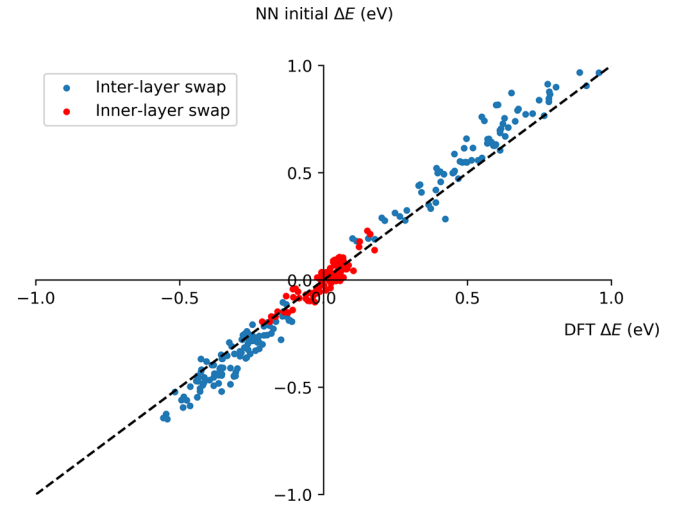


Figure 8. Parity plot of the potential energy change before and after atomic swap calculated by NN without surface relaxation and DFT with surface relaxation.

atomic swaps that occur between two layers and within one layer. For the atomic swaps that occur between two layers, the $\Delta E s$ calculated by NN and DFT are always the same sign. Thus, we should observe the same segregation trend with and without relaxation. For the atomic swaps within one layer, some inconsistencies take place in the $\Delta E s$ near the zero point where the magnitude of the $\Delta E s$ is quite small. These kinds of swaps do not influence the surface concentration directly. These results illustrate that the role of surface relaxation is limited in the Monte Carlo simulation through the error cancellation before and after atoms swap. This error cancellation phenomenon also appeared in the AuPd binary alloy. We conclude that the neglect of surface relaxation in this case is not a likely factor in explaining the discrepancies observed.

Vibrational Contribution to the Surface Segregation.

Another possible reason for the discrepancy between the measured and predicted segregation of Pd and Cu is the neglect of vibrational contributions to the Helmholtz free energy, which was reported to be useful to get more accurately simulated Cu–Pd phase behavior. In the Monte Carlo simulations above, one assumption is that the Helmholtz free energy can be approximated by potential energy and configurational entropy. We did not include vibrational contributions to the change in energy. To take it into account,

the Helmholtz free energy including the vibrational contribution was investigated on a 1 × 1 × 7 slab at 1000 K. All the atoms in the unit cell were free to relax, and the final forces on every atom were less than 0.02 eV/Å2. The vibrational frequencies were calculated by a finite difference method with displacement of 0.01 Å. Table 1 summarizes the potential

Table 1. Potential Energy and Helmholtz Free Energy Change for Segregation of Pd in Cu and Cu in Pd

segregation type	Cu ₃ PdCu ₃ to PdCu ₆	Pd ₃ CuPd ₃ to CuPd ₆
DFT potential change (eV)	-0.014	0.146
Helmholtz free energy change (eV)	-0.063	0.168

energy and Helmholtz free energy change for segregation of Pd in Cu and Cu in Pd. We found that the vibrational energy contributions are too small to result in a change in sign of the segregation energies and thus are not likely the source of the discrepancy.

DFT Errors in Alloy Formation Energies. In the MC simulation results, we saw an overestimated segregation of Au to the surface for CuAu alloy. This might be explained by the DFT predictions of the formation energy of the alloys. Table 2^{46–50} summarizes some reported formation energies of AuCu

Table 2. Experimental and DFT Formation Energies for CuAu Alloys

alloy	experimental (meV/atom)	DFT-PBE (meV/atom)	ordered
Cu ₃ Au	-74	-44	$L1_2$
CuAu	-93	-56	$L1_0$
$CuAu_3$	-39	-25	$L1_2$

alloys, in which DFT-PBE predicts much higher formation energies than experimental data. This means it underestimated the interaction between Cu and Au, which could lead to the overestimated surface concentration of Au as we observed in the Monte Carlo simulations. In other words, the energy cost in losing Cu-Au bonds from Au segregating to the surface is overcompensated by the reduction in the surface energy of Au at the surface. This aspect of the discrepancy can only be rectified by more accurate DFT functionals.

There are also inconsistencies between DFT and experimental surface energies of these three metals. In Table 3, the

Table 3. Mean Surface Energy of (111), (100), and (110) Surfaces of Different Metals, in Joules per Square Meter⁵¹

metal	DFT-PBE	experimental
Cu	1.74	1.79 ± 0.19
Pd	1.59	2.00 ± 0.22
Au	0.87	1.51 ± 0.16

mean surface energies of fcc(111), (100), and (110) for Cu, Pd, and Au as calculated by DFT-PBE are underestimated compared to the experimental data.⁵¹ The underestimation for Au is particularly notable and points to nonsystematic errors across this composition space. This discrepancy also may be a possible reason for the failure of DFT to predict the segregation energy. The more specific reasons for the failure of DFT to predict the formation energies of these alloys and the surface energies of these metals need to be studied in the future.

Orientation Dependence of CuPd Surface Segregation Mode. After investigation of the roles of surface relaxation and vibrational contributions in the surface segregation of the CuPd fcc(111) surface, a remaining reason could be the orientation dependency of segregation. The experimental surfaces are not single-crystal fcc(111) surfaces; they are polycrystalline. In a related study on a Cu-Pd thin film it was found that the surface was fcc(111) textured over a broad range of composition, but in the B2 range a seemingly random distribution of surfaces were observed. 14 Thus, it is likely in this work that there may be other surfaces such as fcc(110) and fcc(100) present, including grain boundaries between these surfaces.

It was reported that CuPd shows different segregation behavior on different fcc surfaces such as (111), (110), and (100).⁵² We compare the DFT segregation energies for CuPd fcc(110) and fcc(111) on a $3 \times 3 \times 6$ slab in Table 4. The

Table 4. CuPd Segregation Energy on fcc(111) and fcc(110)

surface	segregation type	surface relax	segregation energy (eV)
fcc(111)	Cu in Pd	no	0.096
fcc(111)	Pd in Cu	no	-0.066
fcc(111)	Cu in Pd	yes	0.051
fcc(111)	Pd in Cu	yes	-0.122
fcc(110)	Cu in Pd	no	0.006
fcc(110)	Pd in Cu	no	-0.018
fcc(110)	Cu in Pd	yes	-0.166
fcc(110)	Pd in Cu	yes	0.007

inclusion of surface relaxation did not change the sign of the surface segregation energy for fcc(111). On fcc(111), Pd tends to segregate on the surface while Cu tends to diffuse inward the bulk. However, for fcc(110), surface relaxation is significant and it can change the sign of the surface segregation energy. Without surface relaxation, the DFT calculation shows the same segregation trend as on the fcc(111) for Cu and Pd. When we take the surface relaxation into account, the surface segregation trend is reversed. This calculation means that the surface segregation of CuPd depends on the orientation of the slab, which is consistent with the recent experimental work where the surface segregation behavior of Cu and Pd is related to the surface environment.⁵²

To study the details of the surface segregation behavior of CuPd on fcc(110), we performed another set of MC simulation on this orientation. As illustrated in Table 4, surface relaxation plays a significant role for the segregation. Thus, we need to include the surface relaxation energy during the MC simulation. Similar to the way in which we model the total potential energy using a NN, we developed another NN with the same architecture to model the surface relaxation energy using 1000 slab configurations. Only the atoms in the top two layers have a contribution to the surface relaxation energy during the training and prediction phase of the NN. Surface relaxation was considered on both sides of the slab during the MC simulation. The segregation profiles for CuPd fcc(110) with and without considering the surface relaxation are shown in Figure 9. We could see a qualitatively different MC simulation result here compared to the fcc(111) result above. Here, CuPd(110) with surface relaxation has the same segregation trend with the experimental result, while the

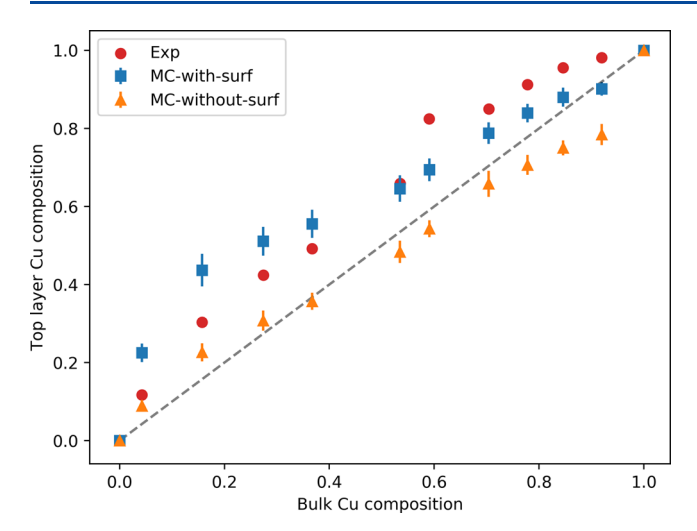


Figure 9. Segregation profile of CuPd(110) at 600 K. Blue squares show the MC simulation results with surface relaxation. Orange triangles show the simulation results without surface relaxation. Red points show the experimental results.³⁸

segregation profile without surface relaxation included is still far away from the experimental result.

In this section, we discussed how the surface orientation affects the segregation profile of CuPd. Due to the complicated surface environment in reality (e.g., step, terraces, and defects), it is not currently possible to fully simulate every detail of all the local environments on a surface. Thus, we only performed a set of MC simulations on fcc(110) to demonstrate that there can be orientation dependent surface segregation behavior of CuPd. Through the comparison between fcc(111) and fcc(110), we have shown that the structure of the surface has significant impact on the segregation profile of CuPd, and this is a probable explanation for the discrepancy between simulation and experiment initially presented in this work as the experimental surfaces are known to be polycrystalline.

CONCLUSIONS

With 5278 fcc(111) slab configurations of PdCuAu, we developed a neural network to compute fcc(111) ternary alloy slab energies and validated its performance. The training samples were selected randomly with or without some constraints on their bulk concentrations. In the fingerprints space we showed that the training set nearly spanned the possible atomic local environments which enable the NN to predict the DFT potential energy of any larger slab encountered in the MC simulation with the MAE of around 2 meV/atom. The trained NN makes it possible to conduct the MC simulation on a $10 \times 10 \times 15$ slab with the first principle potential energy which is computationally unpractical using DFT directly.

Through the combination of NN and MC simulations, the surface concentrations of the slabs with various bulk concentrations were predicted and compared to experimental results. The segregation of Au on the surface was simulated successfully, and the simulation results are qualitatively consistent with the experiments for the AuPd parts of the ternary alloy space. For the CuAu part, the simulation result is qualitatively consistent with the experimental data, but MC simulation overestimated the Au segregation due to the low accuracy of the DFT functional (PBE). In terms of the CuPd part, there are some discrepancies between simulated and

experimentally observed segregation behavior which we ultimately attribute to limitations in the use of ideal fcc(111) surfaces as models for segregation in polycrystalline films. We discussed the orientation dependent surface segregation behavior of CuPd by comparing the simulation results on fcc(111) and fcc(110), and we showed evidence that fcc(110) would show Cu segregation behavior that is more consistent with the experimental observations.

ASSOCIATED CONTENT

Supporting Information

The Supporting Information is available free of charge at https://pubs.acs.org/doi/10.1021/acs.jpcc.1c09647.

Data files needed to reproduce the analysis in this work, scripts used to create the figures from these data files, and additional analysis supporting the conclusions in this work (PDF)

AUTHOR INFORMATION

Corresponding Author

John R. Kitchin — Department of Chemical Engineering, Carnegie Mellon University, Pittsburgh, Pennsylvania 15213, United States; orcid.org/0000-0003-2625-9232; Email: jkitchin@andrew.cmu.edu

Authors

Yilin Yang — Department of Chemical Engineering, Carnegie Mellon University, Pittsburgh, Pennsylvania 15213, United States

Zhitao Guo — Department of Chemical Engineering, Carnegie Mellon University, Pittsburgh, Pennsylvania 15213, United States

Andrew J. Gellman – Department of Chemical Engineering, Carnegie Mellon University, Pittsburgh, Pennsylvania 15213, United States; © orcid.org/0000-0001-6618-7427

Complete contact information is available at: https://pubs.acs.org/10.1021/acs.jpcc.1c09647

Notes

The authors declare no competing financial interest.

ACKNOWLEDGMENTS

This material is based upon work supported by NSF DMREF Award CBET-1921946.

REFERENCES

- (1) Burkhanov, B. G. S.; Gorina, N. B.; Kolchugina, N. B.; Roshan, N. R.; Slovetsky, D. I.; Chistov, E. M. Palladium-Based Alloy Membranes for Separation of High Purity Hydrogen From Hydrogen-Containing Gas Mixtures. *Platinum Metals Review* **2011**, *55*, 3–12.
- (2) Grashoff, G. J.; Pilkington, C. E.; Corti, C. W. The Purification of Hydrogen. *Platinum Met. Rev.* **1983**, 27, 157–169.
- (3) Paglieri, S. N.; Way, J. D. Innovations in Palladium Membrane Research. Separation and Purification Methods 2002, 31, 1–169.
- (4) Zhang, X.; Wang, W.; Liu, J.; Sheng, S.; Xiong, G.; Yang, W. Hydrogen Transport Through Thin Palladium-Copper Alloy Composite Membranes At Low Temperatures. *Thin Solid Films* **2008**, *516*, 1849–1856.
- (5) Shi, L.; Goldbach, A.; Xu, H. High-Flux H₂ Separation Membranes From (Pd/Au)_n Nanolayers. *Int. J. Hydrogen Energy* **2011**, *36*, 2281–2284.
- (6) Zhang, K.; Way, J. D. Palladium-Copper Membranes for Hydrogen Separation. Sep. Purif. Technol. 2017, 186, 39-44.

- (7) Tarditi, A. M.; Imhoff, C.; Braun, F.; Miller, J. B.; Gellman, A. J.; Cornaglia, L. PdCuAu Ternary Alloy Membranes: Hydrogen Permeation Properties in the Presence of H₂S. *J. Membr. Sci.* **2015**, 479, 246–255.
- (8) Honrado Guerreiro, B. M. Palladium-Copper-Gold Alloys for the Separation of Hydrogen Gas. Ph.D. Thesis, Université du Québec, Institut National de la Recherche Scientifique, 2015.
- (9) Burton, J. Surface Segregation in Alloys. J. Catal. 1975, 37, 106–113.
- (10) Chen, M.; Luo, K.; Wei, T.; Yan, Z.; Kuman, D.; Yi, C.; Goodman, D. The nature of the active site for vinyl acetate synthesis over Pd-Au. *Catal. Today* **2006**, *117*, 37–45.
- (11) Calaza, F.; Mahapatra, M.; Neurock, M.; Tysoe, W. T. Disentangling Ensemble, Electronic and Coverage Effects on Alloy Catalysts: Vinyl Acetate Synthesis on Au/Pd(111). *J. Catal.* **2014**, 312, 37–45.
- (12) Bertolini, J.; Rousset, J.; Miegge, P.; Massardier, J.; Tardy, B.; Samson, Y.; Khanra, B.; Creemers, C. Surface Segregation Study of a Dilute Pd₁Fe₉₉ Alloy By LEIS and XPS. *Surf. Sci.* **1993**, *281*, 102–110.
- (13) van den Oetelaar, L. C. A.; Nooij, O. W.; Oerlemans, S.; Denier van der Gon, A. W.; Brongersma, H. H.; Lefferts, L.; Roosenbrand, A. G.; van Veen, J. A. R. Surface Segregation in Supported Pd-Pt Nanoclusters and Alloys. *J. Phys. Chem. B* **1998**, *102*, 3445–3455.
- (14) Priyadarshini, D.; Kondratyuk, P.; Picard, Y. N.; Morreale, B. D.; Gellman, A. J.; Miller, J. B. High-Throughput Characterization of Surface Segregation in Cu_xPd_{1-x} Alloys. *J. Phys. Chem. C* **2011**, *115*, 10155–10163
- (15) Payne, M. A.; Miller, J. B.; Oliveros, M. E.; Perez, G.; Gouvea, C. P.; Archanjo, B. S.; Achete, C. A.; Gellman, A. J. Assessment of a High-Throughput Methodology for the Study of Alloy Oxidation Using $Al_xFe_yNi_{1-x-y}$ Composition Gradient Thin Films. *ACS Comb. Sci.* **2016**, *18*, 425–436.
- (16) Kitchin, J. R.; Gellman, A. J. High-Throughput Methods Using Composition and Structure Spread Libraries. *AIChE J.* **2016**, *62*, 3826–3835.
- (17) Levchenko, E. V.; Evteev, A. V.; Kozubski, R.; Belova, I. V.; Murch, G. E. Molecular Dynamics Simulation of Surface Segregation in a (110) B₂-NiAl Thin Film. *Phys. Chem. Chem. Phys.* **2011**, *13*, 1214–1221.
- (18) Bangwei, Z.; Taglauer, E.; Xiaolin, S.; Wangyu, H.; Huiqiu, D. Simulation Calculations of Surface Segregation for Au-Cu Alloys Using an Analytic Embedded Atom Model. *physica status solidi (a)* **2005**, 202, 2686–2699.
- (19) Tsai, H.-C.; Yu, T. H.; Sha, Y.; Merinov, B. V.; Wu, P.-W.; Chen, S.-Y.; Goddard, W. A. Density Functional Theory Study of Pt₃M Alloy Surface Segregation With Adsorbed O/OH and Pt₃Os As Catalysts for Oxygen Reduction Reaction. *J. Phys. Chem. C* **2014**, *118*, 26703–26712.
- (20) Wynblatt, P.; Landa, A. Computer Simulation of Surface Segregation in Ternary Alloys. *Comput. Mater. Sci.* **1999**, *15*, 250–263.
- (21) Aspera, S. M.; Arevalo, R. L.; Nakanishi, H.; Kasai, H. First Principles Study of Surface Stability and Segregation of PdRuRh Ternary Metal Alloy System. *Surf. Sci.* **2018**, *671*, 51–59.
- (22) Behler, J. Perspective: Machine Learning Potentials for Atomistic Simulations. J. Chem. Phys. 2016, 145, 170901.
- (23) Reveil, M.; Clancy, P. Classification of Spatially Resolved Molecular Fingerprints for Machine Learning Applications and Development of a Codebase for Their Implementation. *Molecular Systems Design & Engineering* **2018**, *3*, 431–441.
- (24) Hu, D.; Xie, Y.; Li, X.; Li, L.; Lan, Z. Inclusion of Machine Learning Kernel Ridge Regression Potential Energy Surfaces in On-The-Fly Nonadiabatic Molecular Dynamics Simulation. *J. Phys. Chem. Lett.* **2018**, *9*, 2725–2732.
- (25) Peterson, A. A.; Christensen, R.; Khorshidi, A. Addressing Uncertainty in Atomistic Machine Learning. *Phys. Chem. Chem. Phys.* **2017**, *19*, 10978–10985.

- (26) Behler, J.; Parrinello, M. Generalized Neural-Network Representation of High-Dimensional Potential-Energy Surfaces. *Phys. Rev. Lett.* **2007**, *98*, 146401.
- (27) Boes, J. R.; Kitchin, J. R. Modeling Segregation on AuPd(111) Surfaces With Density Functional Theory and Monte Carlo Simulations. J. Phys. Chem. C 2017, 121, 3479—3487.
- (28) Onat, B.; Cubuk, E. D.; Malone, B. D.; Kaxiras, E. Implanted Neural Network Potentials: Application To Li-Si Alloys. *Phys. Rev. B* **2018**, *97*, 094106.
- (29) Tarditi, A.; Bosko, M.; Cornaglia, L. Comprehensive Materials Finishing; Comprehensive Materials Finishing; Elsevier, 2017; pp 1-24.
- (30) Artrith, N.; Kolpak, A. M. Understanding the Composition and Activity of Electrocatalytic Nanoalloys in Aqueous Solvents: a Combination of DFT and Accurate Neural Network Potentials. *Nano Lett.* **2014**, *14*, 2670–2676.
- (31) Kresse, G.; Hafner, J. Ab Initio molecular Dynamics for Liquid Metals. *Phys. Rev. B* **1993**, *47*, 558–561.
- (32) Kresse, G.; Furthmüller, J. Efficiency of Ab-Initio Total Energy Calculations for Metals and Semiconductors Using a Plane-Wave Basis Set. *Comput. Mater. Sci.* **1996**, *6*, 15–50.
- (33) Blöchl, P. E. Projector Augmented-Wave Method. *Phys. Rev. B* **1994**, *50*, 17953–17979.
- (34) Kresse, G.; Joubert, D. From Ultrasoft Pseudopotentials To the Projector Augmented-Wave Method. *Phys. Rev. B* **1999**, *59*, 1758–1775.
- (35) Perdew, J. P.; Burke, K.; Ernzerhof, M. Generalized Gradient Approximation Made Simple. *Phys. Rev. Lett.* **1996**, *77*, 3865–3868.
- (36) Perdew, J. P.; Burke, K.; Ernzerhof, M. Generalized Gradient Approximation Made Simple [phys. Rev. Lett. 77, 3865 (1996)]. *Phys. Rev. Lett.* **1997**, 78, 1396–1396a.
- (37) Monkhorst, H. J.; Pack, J. D. Special Points for Brillouin-Zone Integrations. *Phys. Rev. B* **1976**, *13*, 5188–5192.
- (38) Yin, C.; Guo, Z.; Gellman, A. J. Surface Segregation Across Ternary Alloy Composition Space: Cu_xAu_yPd_{1-x-y}. *J. Phys. Chem. C* **2020**, *124*, 10605–10614.
- (39) Behler, J. Atom-Centered Symmetry Functions for Constructing High-Dimensional Neural Network Potentials. *J. Chem. Phys.* **2011**, *134*, 074106.
- (40) Artrith, N.; Behler, J. High-Dimensional Neural Network Potentials for Metal Surfaces: a Prototype Study for Copper. *Phys. Rev. B* **2012**, *85*, 045439.
- (41) Khorshidi, A.; Peterson, A. A. Amp: a Modular Approach To Machine Learning in Atomistic Simulations. *Comput. Phys. Commun.* **2016**, 207, 310–324.
- (42) Bahn, S.; Jacobsen, K. An Object-Oriented Scripting Interface To a Legacy Electronic Structure Code. Computing in Science & Engineering 2002, 4, 56–66.
- (43) Larsen, A. H.; Mortensen, J. J.; Blomqvist, J.; Castelli, I. E.; Christensen, R.; Dułak, M.; Friis, J.; Groves, M. N.; Hammer, B.; Hargus, C.; et al. The Atomic Simulation Environment-A Python Library for Working With Atoms. *J. Phys.: Condens. Matter* **2017**, *29*, 273002.
- (44) Vegard, L. Die Konstitution Der Mischkristalle Und Die Raumfllung Der Atome. Zeitschrift fr Physik 1921, 5, 17–26.
- (45) Tanner, P. Ordering and Segregation in the PdAuCu System: Bulk vs. Surface. M.Sc. Rhesis, Chalmers University of Technology, 2019.
- (46) Geng, F.; Boes, J. R.; Kitchin, J. R. First-Principles Study of the Cu-Pd Phase Diagram. *Calphad* **2017**, *56*, 224–229.
- (47) Meschel, S.; Kleppa, O. Thermochemistry of Some Binary Alloys of Noble Metals (Cu, Ag, Au) and Transition Metals By High Temperature Direct Synthesis Calorimetry. *J. Alloys Compd.* **2003**, 350, 205–212.
- (48) Sluiter, M. H. F.; Colinet, C.; Pasturel, A. Ab Initio Calculation of the Phase Stability in Au-Pd and Ag-Pt Alloys. *Phys. Rev. B* **2006**, 73, 174204.
- (49) Li, M.; Du, Z.; Guo, C.; Li, C. A Thermodynamic Modeling of the Cu-Pd System. *Calphad* **2008**, *32*, 439–446.

- (50) Zhang, Y.; Kresse, G.; Wolverton, C. Nonlocal First-Principles Calculations in Cu-Au and Other Intermetallic Alloys. *Phys. Rev. Lett.* **2014**, *112*, 075502.
- (51) Patra, A.; Bates, J. E.; Sun, J.; Perdew, J. P. Properties of Real Metallic Surfaces: Effects of Density Functional Semilocality and Van Der Waals Nonlocality. *Proc. Natl. Acad. Sci. U. S. A.* **2017**, *114*, E9188–E9196.
- (52) Pielsticker, L.; Zegkinoglou, I.; Han, Z.-K.; Navarro, J. J.; Kunze, S.; Karslıoğlu, O.; Levchenko, S. V.; Cuenya, B. R. Crystallographic Orientation Dependence of Surface Segregation and Alloying on PdCu Catalysts for CO₂ Hydrogenation. *J. Phys. Chem. Lett.* **2021**, *12*, 2570–2575.

□ Recommended by ACS

Understanding and Modifying the Scaling Relations for Ammonia Synthesis on Dilute Metal Alloys: From Single-Atom Alloys to Dimer Alloys

Yining Zhang, Jiannian Yao, et al.

JULY 15, 2022 ACS CATALYSIS

READ 🗹

Combinatorial High-Throughput Methods for Designing Hydrogen Evolution Reaction Catalysts

Xuanzhi Liu, Jun-Qiang Wang, et al.

MARCH 11, 2022 ACS CATALYSIS

READ 🗹

Alloy Catalyst Design beyond the Volcano Plot by Breaking Scaling Relations

Chukwudi F. Nwaokorie and Matthew M. Montemore

FEBRUARY 16, 2022

THE JOURNAL OF PHYSICAL CHEMISTRY C

READ 🗹

Machine Learning-Assisted Screening of Stepped Alloy Surfaces for C₁ Catalysis

Xinyan Liu, Tao Wang, et al.

MARCH 25, 2022

ACS CATALYSIS

READ 🗹

Get More Suggestions >